Journal of Hazardous Materials 188 (2011) 341–349

Contents lists available at ScienceDirect

Journal of Hazardous Materials

journal homepage: www.elsevier.com/locate/jhazmat

Characterization of Co-doped birnessites and application for removal of lead and arsenite

Hui Yin, Xionghan Feng, Guohong Qiu, Wenfeng Tan, Fan Liu*

Key Laboratory of Subtropical Agriculture Resource and Environment, Ministry of Agriculture, Huazhong Agricultural University, No. 1 Nanhu Shizishan Street, Wuhan, 430070, PR China

ARTICLE INFO

Article history:
Received 20 August 2010
Received in revised form
22 December 2010
Accepted 29 January 2011
Available online 4 February 2011

Keywords:
Manganese dioxide
Birnessite
Cobalt doping
Lead adsorption
Arsenite removal

ABSTRACT

Nanostructured Co-doped birnessites were successfully synthesized, and their application for the removal of Pb^{2+} and As(III) from aquatic systems was investigated. Powder X-ray diffraction, chemical analysis, nitrogen physical adsorption, field emission scanning electron microscopy (FE-SEM) and X-ray photoelectron spectroscopy (XPS) were used to characterize the crystal structure, chemical composition, micromorphologies and surface properties of the birnessites. Doping cobalt into the layer of birnessite had little effect on its crystal structure and micromorphology. Both chemical and XPS analyses showed that the manganese average oxidation state (Mn AOS) decreased after cobalt doping. The Co dopant existed mainly in the form of Co(III)OOH in the birnessite structure. Part of the doped Co^{3+} substituted for Mn^{4+}, resulting in the gain of negative charge of the layer and an increase in the content of the hydroxyl group, which accounted for the improved Pb^{2+} adsorption capacity. The maximum capacity of Pb^{2+} adsorption on HB, CoB5, CoB10 and CoB20 was 2538 mmol kg^{-1}, 2798 mmol kg^{-1}, 2932 mmol kg^{-1} and 3146 mmol kg^{-1}, respectively. The total As(III) removal from solution was 94.30% for CoB5 and 100% for both CoB10 and CoB20, compared to 92.03% for undoped HB, by oxidation, adsorption and fixation, simultaneously.

1. Introduction

Manganese oxide octahedral molecular sieves (OMS) have been widely used in oxidation catalysts, absorbents, semiconductor and electrochemical materials due to their special layered or porous structure, mixed valence of manganese and specific physicochemical properties, among others [1–6].

Incorporation of various transition metal ions into the framework of manganese oxides by doping with cations is an effective route to enhance the properties of these materials. Zhou et al. successfully doped first row transition metal ions into the framework of todorokite (OMS-1) and cryptomelane (OMS-2). Both the conversion and selectivity of the oxidative dehydrogenation of ethanol over each individual OMS material are highly dependent on the nature of the dopants. The [Co]-OMS-1 materials possess the highest conversion and selectivity in the catalysis of acetaldehyde oxidation among all the materials [7]. The OMS-2 doped with various ions has a higher surface area and pore volume and lower thermal stability compared to undoped analogies [8]. The resistivity, thermal stability and crystallinity of Tungsten-doped OMS-2 are closely related with the amount of exotic ions [9]. The Co substitution for Mn in nanostructured birnessite and cryptomelane leads to the improvement of their catalytic activity with respect to olefin oxidation and significantly impacts their electrode performances [10]. Doping with Co in K-birnessite prepared by calcination and aqueous treatment improves the discharge–recharge capacity and capacity retention in an aprotic Li cell [11]. Bi^{3+} and Pb^{2+} modification facilitates a significantly longer cycle life for birnessite operating in alkaline cells [12,13]. However, these literatures are mainly focused on the fabrication and characterization of doped materials and their application to catalysts for organic oxidation, sensors and cathode fields. Few reports are on the application of modified manganese oxides in the adsorption and oxidation of toxic metal ions from polluted aquatic systems.

Birnessite possesses a layered structure of edge-sharing [MnO_6] octahedra alternating with water layers with either Na^+ or K^+ in the interlayer. Some of the octahedra are vacant, and H^+ and Mn^{3+}/Mn^{2+} are localized above and/or below these sites [14]. Here, birnessite was synthesized by the reaction of mixed, concentrated hydrochloride and cobalt chloride with potassium permanganate solutions at 100 °C at atmospheric pressure for no more than 1.5 h. Owing to their similar sizes and charges, cobalt can substitute for manganese in the layers. However, the electronegativity of cobalt in various crystallographic situations is different from those of manganese, and the Co^{3+}/Co^{2+} redox conjugate pair has a greater standard redox potential than those of $MnO_2/Mn^{3+}/Mn^{2+}$. Thus, the

* Corresponding author. Tel.: +86 27 87280271; fax: +86 27 87280271.
E-mail address: liufan@mail.hzau.edu.cn (F. Liu).

0304-3894/$ – see front matter © 2011 Elsevier B.V. All rights reserved.
doi:10.1016/j.jhazmat.2011.01.129

purpose of this paper is to investigate the effects of cobalt doping on the crystal structure, morphology, Mn AOS, layer charge and the abundance of hydroxyl groups in the birnessite, the resulting removal of Pb^{2+} and As(III) from aquatic systems, and to discuss the underlying mechanisms. It is helpful to further understand the interaction of manganese oxides with cobalt, the effects of cobalt on the reactivity of manganese oxides, and to synthesize novel environmentally friendly nanoscale manganese oxide materials doped with other transition metal ions in practice.

2. Materials and methods

2.1. Sample preparation

Nanocrystalline Co-doped birnessite was prepared according to McKenzie's method [15]. Mixtures of 45 mL of 6 mol L^{-1} HCl and $CoCl_2$ were added dropwise at a constant velocity of 0.7 mL min^{-1} into a boiling solution of 300 mL of 0.667 mol L^{-1} $KMnO_4$ with vigorous stirring. After boiling for a further 30 min, the suspension was cooled naturally and then aged at 60 °C overnight. The obtained powder was washed thoroughly with DDW and then dried at 40 °C.

Based on the initial molar ratios of Co/Mn, the products were named HB, CoB5, CoB10 and CoB20.

2.2. Lead adsorption experiments

The Pb^{2+} adsorption experiments were conducted at a constant supporting electrolyte concentration ($NaNO_3$, I_c = 0.1 mol L^{-1}). An aliquot of 0–10 mL of 15 mmol L^{-1} $Pb(NO_3)_2$ (pH = 5 ± 0.05) was pipetted into a series of 50-mL polyethylene tubes; then the $NaNO_3$ solution was added to fill the volume up to 10 mL. An aliquot of 5 mL of 5 g L^{-1} Co-doped birnessite suspension, which was pre-equilibrated to a pH level of 5, was added into each tube, followed by shaking at 250 r/min for 24 h at 25 °C. The pH of the reaction system was maintained at 5.00 ± 0.05 using a pH-stat technique. At the end of the reaction, the mixtures were centrifuged, and the supernatants were collected for Pb^{2+}, Mn^{2+}, Co^{2+} and K^+ analyses by atomic absorption spectrometry (AAS, Varian AAS 240FS) and flame spectrometry (Sherwood Model 410) [16].

2.3. As(III) transformation

The As(III) transformation was carried out at 25 °C while stirring. A quantity of 0.1250 g of birnessite was suspended in 150 mL of 0.1 mol L^{-1} $NaNO_3$ for 12 h to eliminate the effect of stirring and surface aquotization, and the pH was adjusted to 7. A volume of 100 mL of a 0.2 mmol L^{-1} $NaAsO_2$ solution (pH = 7, containing 0.1 mol L^{-1} $NaNO_3$) was quickly poured into the suspension to initiate the reaction. An aliquot of 10 mL of the mixtures was withdrawn and immediately filtered through a 0.45-μm membrane at intervals to investigate the kinetics of the oxidation. After reacting for 7 h, the spent mineral was immediately collected by centrifugation, washed with DDW and then dried at 60 °C overnight. One portion of the spent mineral was analyzed by X-ray diffraction and XPS. The other portion was extracted by 0.1 mol L^{-1} NaOH for 24 h [17]. The total As in solution was detected by hydride generation-atomic absorption spectrometry [18]. As(V) was measured using the colorimetric method described by Oscarson et al. [19].

2.4. Characterization

2.4.1. Powder X-ray diffraction

The crystal structures of the Co-doped manganese oxides were characterized by powder XRD measurements carried out on a Bruker D8 Advance diffractometer equipped with a LynxEye detector using Ni-filtered Cu Kα radiation (λ = 0.15406 nm). The diffractometer was operated at a tube voltage of 40 kV and a current of 40 mA with a scanning rate of 1°/min at a step size of 0.02°.

2.4.2. Elemental analysis and Mn AOS

The chemical composition of the samples was determined as follows: 0.1000 g of sample was dissolved in 25 mL of 0.25 mol L^{-1} $NH_2OH{\cdot}HCl$ and 1 mol L^{-1} H_2SO_4. The content of the metal ions was measured using AAS and flame spectrophotometry.

The Mn AOS was obtained by a titration method [20]. A mass of 0.2000 g birnessite was completely reduced to Mn^{2+} in 5 mL of 0.5000 mol L^{-1} $H_2C_2O_4$ and 10 mL of 1 mol L^{-1} H_2SO_4. Excess $C_2O_4^{2-}$ was determined by back-titration using a $KMnO_4$ standard solution at 75 °C.

2.4.3. Specific surface area

The specific surface area (SSA) was examined by nitrogen adsorption at liquid nitrogen temperature using an Autosorb-1 standard physical adsorption analyzer (Quantachrome Autosorb-1, JEDL-6390/LV). The samples were degassed at 110 °C for 3 h under vacuum prior to the adsorption measurement.

2.4.4. Field emission scanning electron microscopy

The crystallite morphologies of samples were probed by field emission scanning electron microscopy with a Jeol JSM-6700F microscope after being coated with a gold evaporated film.

2.5. X-ray photoelectron spectroscopy

X-ray photoelectron spectra were collected using a VG Multilab2000 X-ray photoelectron spectrometer with an Al Kα X-ray source (1486 eV) and a base pressure of 3×10^{-9} Torr in the analytical chamber. The scans were recorded using the large area mode. The survey scans were collected using a fixed pass energy of 100 eV and an energy step size of 1.0 eV, whereas the narrow scans has a pass energy of 25 eV and an energy step size of 0.1 eV. The charge effect was corrected by adjusting the binding energy (BE) of C (1s) to 284.62 eV. The spectra were analyzed using the Avantage software. The Shirley-type background was subtracted before deconvolution and fitting. The parameters used by Nesbitt et al. [21] for the multiplet peaks of Mn ($2p_{3/2}$) for spectra fitting were adopted. A 20:80 ratio of the Lorentzian:Gaussian mix-sum function was used for all the fittings.

3. Results and discussion

3.1. Crystal structure of the Co-doped birnessites

Fig. 1 shows the powder XRD patterns of the obtained samples. The results agree well with JCPDS 86-0666 (hexagonal, $R\bar{3}m$). Birnessite is characterized by four detectable peaks: 0.723 nm, 0.361 nm, 0.244 nm and 0.142 nm. Both peaks at 0.723 nm and 0.361 nm are symmetrical, while the other two at the higher angles are greatly widened. The *d* value ratio of the 0.244-nm peak to the 0.142 nm-peak is close to 1.732, indicating a hexagonal symmetry.

Co-doped birnessites have the same XRD profile as the undoped sample. There are four peaks with similar symmetry and relative intensity. As the initial molar ratios of Co/Mn increase, no extra peaks are detected, which proves that the incorporation of cobalt into the lamellar birnessite did not change the crystal structure, and no second phase was introduced. After Co^{2+} was added, it was immediately oxidized to Co^{3+} by MnO_4^-. Besides similar sizes and charges, both cobalt and manganese are generally stabilized in layered structures composed of edge-sharing octahedra of Mn^{3+} and/or Mn^{4+} to be replaced by newly formed Co^{3+}. However, there was some tiny change in the profiles, especially in the strongest reflection. As the content of cobalt increases, the intensity of the

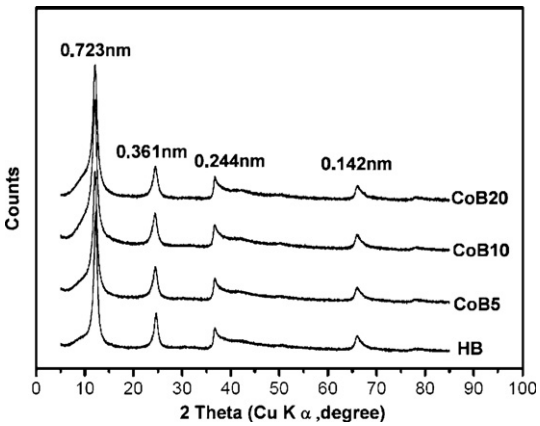

Fig. 1. Powder XRD patterns of birnessite and Co-doped birnessites.

0.723-nm reflection becomes weaker, and its FWHM increases. This result indicates a smaller particle size and weaker crystallinity.

3.2. Elemental analyses and Mn AOS

The results of the elemental analyses are listed in Table 1. There is good agreement between the experimental cobalt percentage determined by AAS and the initial cobalt content. As the initial Co/Mn molar ratios are 0.05, 0.1 and 0.2, the final values of the obtained products are 0.06, 0.12 and 0.22, respectively. The content of potassium remains almost constant in both undoped and doped birnessites, except for the slight decrease in CoB20, which indicates that some cobalt may exist in the interlayer by replacing K^+. Sample HB has 52.74% Mn in weight. The Mn content of Co-doped birnessites decreases. The percentages of Mn in CoB5, CoB10 and CoB20 are 51.26%, 48.85% and 45.68%, respectively. Table 1 also shows that the increasing cobalt content correlates well with the decrease in the Mn percentage and a relatively constant K concentration, indicating that cobalt is isomorphously substituting for Mn in the layer rather than replacing K^+ in the interlayer.

It can be concluded that if Mn^{3+} is substituted by Co^{3+}, then there is no charge gain. Conversely, the increase in the negative layer charge of birnessite will be caused by the substitution of Co^{3+} for Mn^{4+}.

The Mn AOS of samples are also calculated (Table 1). Co-free birnessite has an AOS of 3.78, confirming that both Mn^{3+} and Mn^{4+} are present in the structure with Mn^{4+} being the predominant species. With increasing cobalt content, the Mn AOS of Co-doped birnessites gradually decreases and reaches the lowest value of 3.71 for CoB20.

There are two reasons for this result. First, the coordination radius, crystal field stabilization energy (CFSE) and oxidation state are the crucial factors for substitution. Manganese exists mainly in a high-spin (HS) state in its oxides and hydroxides. Conversely, all octahedral complexes of Co^{3+}, with the exception of the fluoride, are low spin [22]. The coordination radius of low-spin Co^{3+} (0.685 Å) is closer to that of Mn^{4+} (0.67 Å) than Mn^{3+} (0.785 Å) [23], and the CFSE of low-spin Co^{3+} is higher than that of Mn^{4+} [24]. The substitution of some Mn^{4+} by Co^{3+} is favorable in the preparation process, resulting in more Mn^{3+} relative to Mn^{4+} in the Co-doped birnessites. Second, although the amount of MnO_4^- was equal and relatively sufficient in the reactants with the increase of the Co/Mn molar ratio, the moles of reductant (Co^{2+}, Cl^-) gradually increased, such that it would not rule out that some low valence cations remain unoxidized, resulting in the increase in the percentage of Mn^{3+}. Some Co^{2+} existing in the CoB20, as illustrated in Fig. 5, is more evidence of this possibility.

3.3. Specific surface area analyses

The SSAs of the samples are listed in Table 1. HB has a specific surface area of 19.26 $m^2\,g^{-1}$. Those of the Co-doped samples first increased and then decreased. The surface areas of CoB5, CoB10, and CoB20 are 27.43 $m^2\,g^{-1}$, 17.16 $m^2\,g^{-1}$ and 10.28 $m^2\,g^{-1}$, respectively. As indicated by XRD analysis, the crystallinity of Co-doped samples gradually decreased. The weaker the crystallinity of the sample, the more serious is the aggregation that occurs [10]. The aggregation of fine crystals may be one reason for the decrease in SSA. Otherwise, with the increase in hydroxyl groups, the polarity of the mineral surface increased, and the adsorption of nonpolar molecular N_2 would be possibly hindered and decreased during SSA measurements by the BET method.

3.4. Micromorphology

As illustrated in Fig. 2, the FE-SEM analysis clearly demonstrates the formation of three-dimensional (3D) hierarchical microspheres consisting of two-dimensional (2D) nanoplates. The thickness of the 2D nanoplates is approximately 10 nm or even thinner, and the radius of the 3D microspheres is approximately 200–300 nm.

Cobalt doping has no apparent effect on the micromorphologies of the products. In the whole range of the Co/Mn ratios, all the samples have the same morphology. Both the 2D nanoplates and 3D microspheres are uniform, indicative of the presence of only one phase [21], which is clearly proved by powder XRD.

3.5. Surface characterization using XPS

X-ray photoelectron spectroscopy is now a widely used analytical technique for investigating the abundance and chemical state of elements in the uppermost few atomic layers of solid surfaces. Fig. S1 shows the broad scans of the samples. The peak at a BE of 780 eV in the scans is the photoelectron line of cobalt, and its intensity gradually increases with increasing Co. The photoelectron line of K (2p) is at the left of C (1s). Its relative intensity is unchanged in HB, CoB5 and CoB10, but weaker in CoB20, suggesting a lower abundance of potassium in CoB20. This coincides with the results of the chemical analysis.

Narrow scans of Mn, Co and O in the layered materials were also taken. The BEs of Mn (2p), Co (2p) and O (1s) are listed in Table 2.

The BEs of Mn ($2p_{1/2}$) and Mn ($2p_{3/2}$) of HB are 653.93 eV and 642.32 eV, respectively. These values for Co-doped materials shift to the low BE side, indicating a decrease in the Mn AOS. Since Mn^{2+}, Mn^{3+} and Mn^{4+} have essentially the closest and overlapped BEs, it is difficult to directly identify the oxidation state of manganese only

Table 1
Elemental analysis, SSA and Mn AOS of Co-doped birnessites.

Sample	Element content (%)			Co/Mn molar ratio	Mn AOS	SSA ($m^2\,g^{-1}$)
	Mn	Co	K			
HB	52.74	0	8.36	0	3.78	19.26
CoB5	51.26	3.46	8.25	0.06	3.75	27.43
CoB10	48.85	6.23	8.20	0.12	3.74	17.16
CoB20	45.68	10.72	7.98	0.22	3.71	10.28

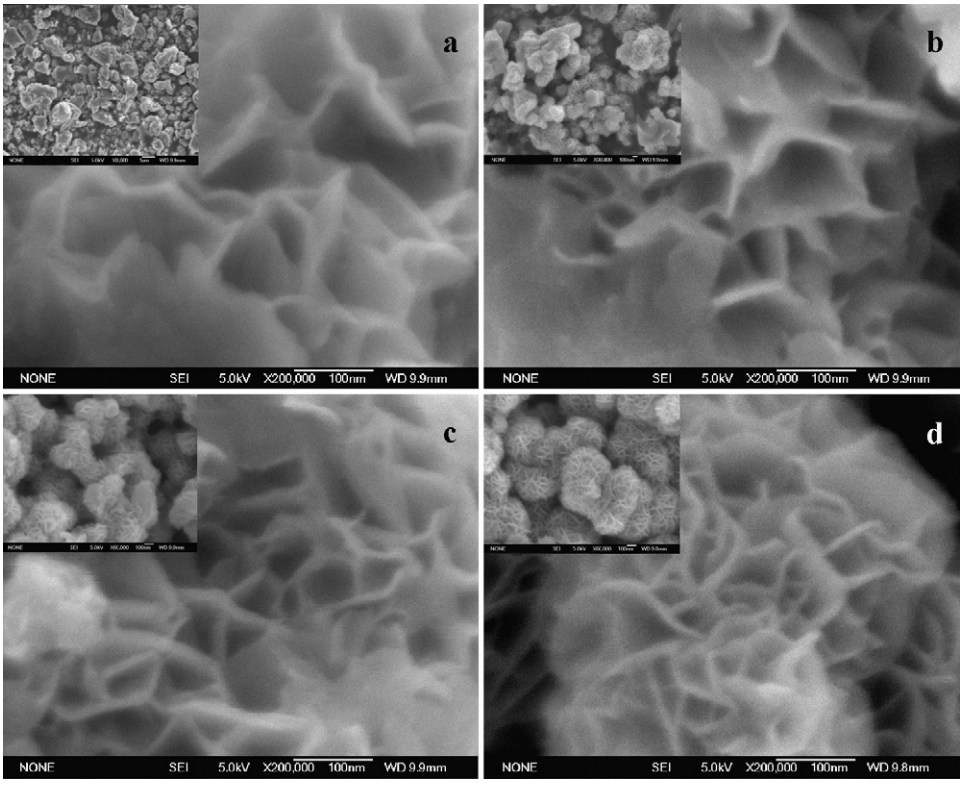

Fig. 2. FE-SEM images of Co-doped birnessites. a: HB; b: CoB5; c: CoB10; d: CoB20.

by the BEs of Mn (2p) [25]. Therefore, fitting of Mn ($2p_{3/2}$) was carried out.

The fitting results are listed in Fig. 3 and Table 3. The percentages of Mn^{2+}, Mn^{3+} and Mn^{4+} in HB are 1.20%, 16.07% and 82.74%, respectively. The content of Mn^{3+} in doped samples increases, whereas that of Mn^{4+} decreases. According to the fitting results, the calculated Mn AOS are 3.82, 3.75, 3.71 and 3.58 for HB, CoB5, CoB10 and CoB20, respectively. These values are negatively correlated with the content of cobalt. Although XPS detects only the information of the surface, the consistence of its results with the titration results indicates the uniform bulk composition of all the samples.

Narrow scans of Co (2p) were plotted in Fig. 4. The measured BEs for Co ($2p_{1/2}$) and Co ($2p_{3/2}$) are 795 eV (±0.05 eV) and 780 eV (±0.15 eV), respectively, equal to those of Co(III)OOH reported by Crowther et al. [26]. The Co ($2p_{1/2}$)–Co ($2p_{3/2}$) splittings are also identical at 15.0 eV (±0.20 eV). It is suggested that Co(III) exclusively exists in the samples. However, when the initial Co/Mn molar ratio was high, the BE of the two split peaks shifted to the low BE side, and shake-up satellite peaks appeared on the high BE sides of each. This result means that CoB20 may contain a small amount of Co(II) [27,28]. Additionally, the Co ($2p_{1/2}$)–Co ($2p_{3/2}$) splittings of CoB20 are 15.4 eV between the values of Co(III) (15 ± 0.1 eV) and Co(II) (15.9 ± 0.1 eV) [26]. This is only more proof of the presence of Co(II) in CoB20.

Therefore, the Mn (2P) and Co (2P) spectra indicate the presence of Mn^{2+} and Co^{2+} on the surface of Co-doped birnessites although the molar ratio of Mn(VII) to Co(II) is much higher than that of the equivalent molar ratio. The formation of Co-doped birnessites occurred in multiple, compositional, heterogeneous systems, and the mechanisms are very complicated.

Permanganate in solution is intrinsically unstable, decomposes slowly, but is observable in acidic solution [29].

$$4MnO_4^- + 4H^+ \rightarrow 3O_2(g) + 2H_2O + 4MnO_2(s)$$

Manganese dioxide is inert to most acids except when heated. Under the conditions here, both $KMnO_4$ and MnO_2 can react with HCl as follows [29]:

$$KMnO_4 + HCl \rightarrow MnCl_2 + Cl_2(g) + H_2O$$

$$MnO_2 + HCl \rightarrow MnCl_2 + Cl_2(g) + H_2O$$

Newly formed Mn^{2+} in the above reaction and the yet unoxidized Co^{2+}, especially in CoB20 for the highest content in the initial mixtures, can be captured into birnessite during its formation. Once these ions are incorporated into the layer, further oxidation will be hindered, thus retaining the structure.

Table 2
BE values for Mn (2p), Co (2p) and O (1s) (eV).

Sample	Mn ($2p_{1/2}$)	Mn ($2p_{3/2}$)	Co ($2p_{3/2}$)	ΔBE Co ($2p_{1/2}$)–Co ($2p_{3/2}$)	O 1s
HB	653.93	642.32			529.76
CoB5	653.66	641.68	780.09	14.92	529.34
CoB10	653.55	641.77	779.86	15.14	529.29
CoB20	653.49	641.59	779.58	15.38	529.21
CoOOH[a]			780.20	15.10	
$Co(OH)_2$[a]			781.0	15.90	

[a] Values from Crowther et al. [26].

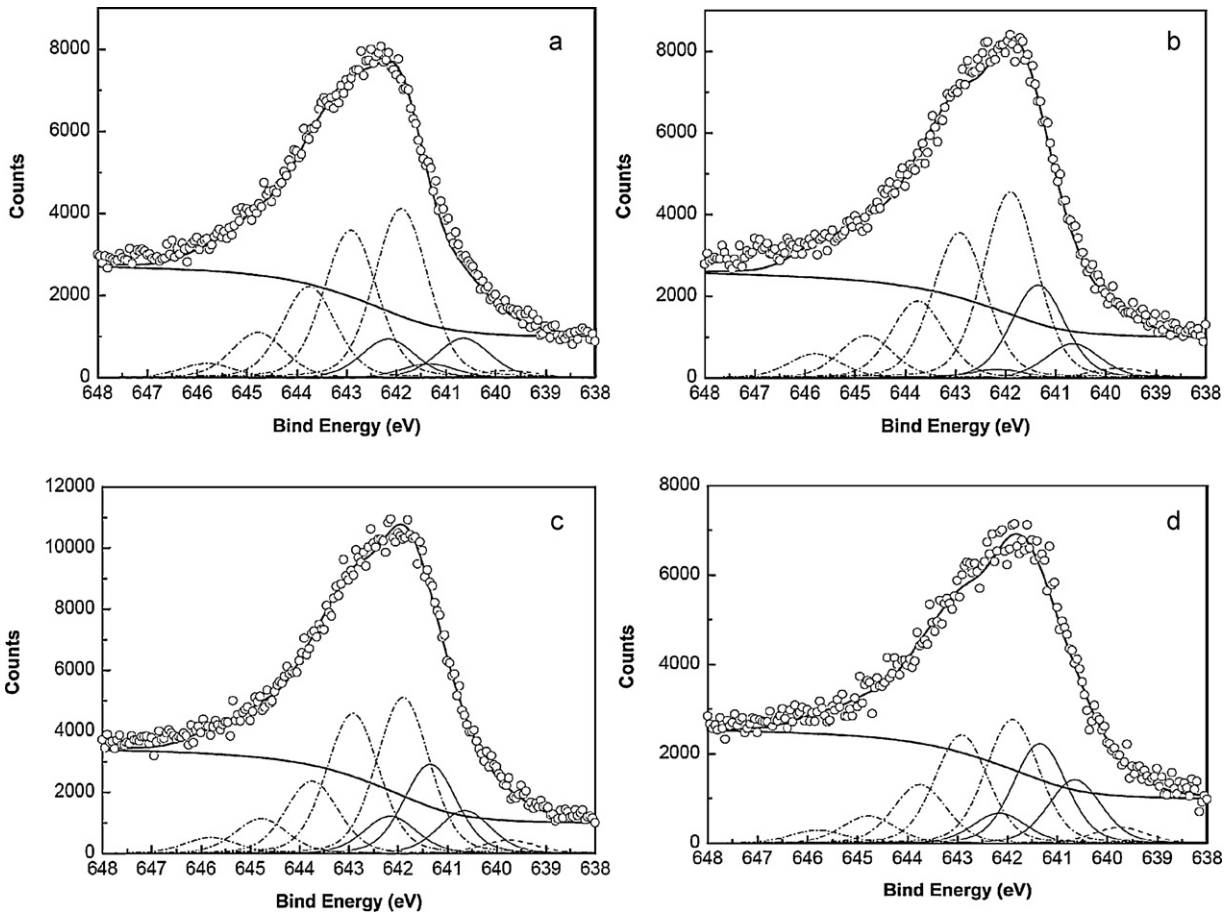

Fig. 3. Mn ($2p_{3/2}$) spectra of Co-doped birnessites. a: HB; b: CoB5; c: CoB10; d: CoB20 (The upper circles represent the observed data, and the thick, solid curve is the best fit of the data. The dash-dot curves represent Mn(IV) multiplet peaks, while the thin, solid curves are Mn(III) and the dotted lines are Mn(II)).

Table 3
Near-surface compositions of Mn and O species derived from fittings of Mn ($2p_{3/2}$) and O (1s).

Sample	Mn (At.%)			O (At.%)		
	Mn^{2+}	Mn^{3+}	Mn^{4+}	O^{2-}	OH^-	H_2O
HB	1.20	16.07	82.74	73.22	12.79	13.98
CoB5	1.52	21.75	76.73	67.59	13.05	19.36
CoB10	2.17	29.10	69.73	68.52	17.69	13.79
CoB20	2.92	35.71	61.37	62.39	17.79	19.82

The asymmetry of the profiles of O (1s) demonstrates the multiplex contributions to the spectrum. The O (1s) spectrum of undoped birnessite has a main peak near 529.8 eV with a broad shoulder on the high BE side and a pronounced tail. Co-doped samples have the same shape as HB, but their main peaks shift to 529.3 eV (±0.1 eV), the broad shoulders and tails also exist.

There are mainly three species of oxygen existing in manganese oxides: lattice oxygen (O^{2-}), hydroxide oxygen (OH^-) and oxygen in molecular water (physisorbed, chemisorbed, and structural H_2O and water in poor electrical contact with the mineral surface) [30], corresponding to the main peak, the broad shoulder and the pronounced tail, respectively. As illustrated above, the percentage of Mn^{3+} in Co-doped birnessites increases. According to Portier et al. [31], Mn^{3+} (HS, $\chi = 1.675$) and Co^{3+} (LS, $\chi = 1.791$) in the [$Mn(Co)O_6$] octahedra of birnessites are less electronegative than Mn^{4+} (HS, $\chi = 1.923$). Therefore, more Mn^{3+} and Co^{3+} in the layer lead to the increase in the ionic bond character of the Mn(Co)–O and thus the electron cloud density of cores of anions (O^{2-}) and OH^- increases, and their BEs shift to the lower. However, the BE of oxygen in H_2O did not change. The peak parameters used (Table S1) and the results

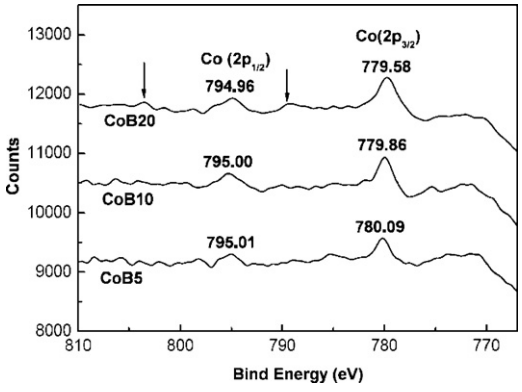

Fig. 4. Co (2p) spectra of Co-doped birnessites.

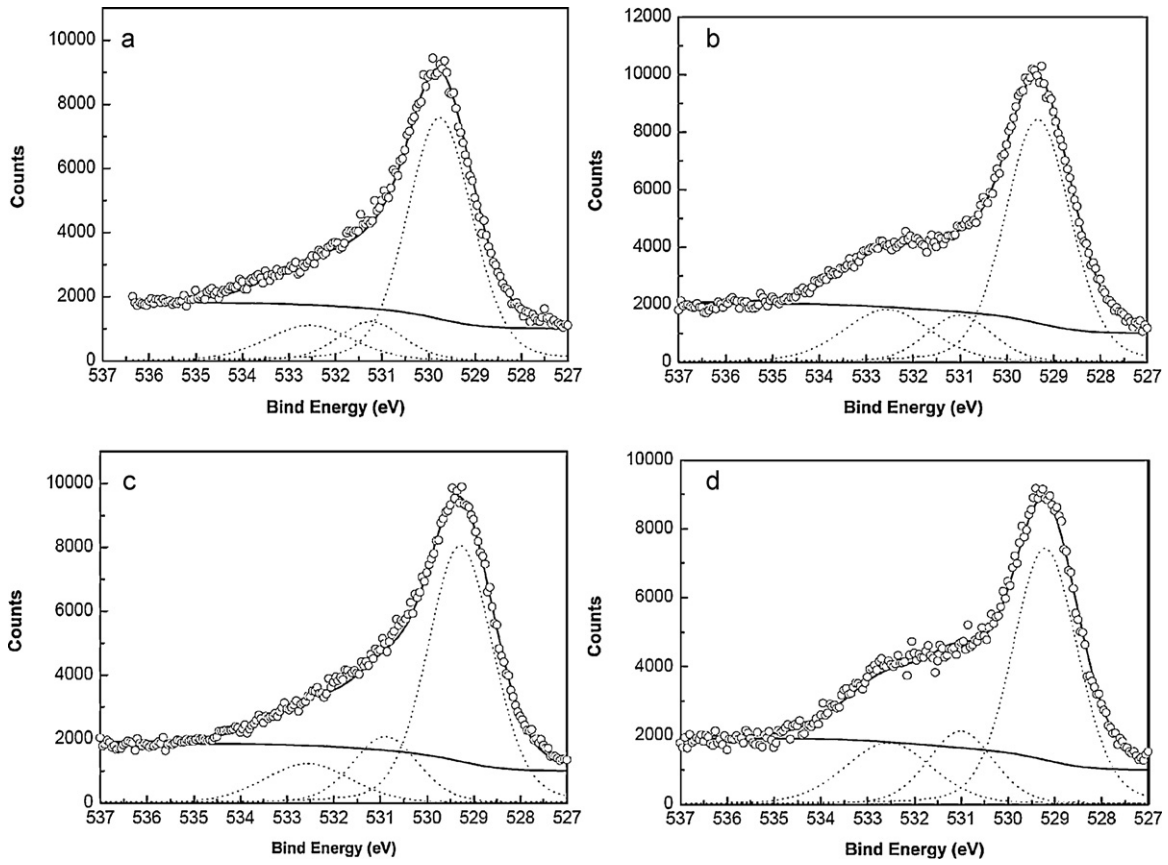

Fig. 5. O (1s) spectra of Co-doped birnessites. a: HB; b: CoB5; c: CoB10; d: CoB20 (The thick, solid curve is the best fit of the spectral data. The dotted curves represent photopeak contributions from O^{2-}, OH^- and H_2O, respectively.).

of fitting the character outside of the O (1s) spectra are listed in Fig. 5 and Table 3. Among the three species of oxygen, the abundance of hydroxide oxygen increases with increasing cobalt. The content of hydroxide oxygen in HB is 12.79%, and those of the doped ones are 13.05%, 17.69% and 17.79%, respectively.

3.6. Adsorption of Pb^{2+} by Co-doped birnessites

Here, isothermal adsorption experiments of Pb^{2+} on birnessite and Co-doped analogs were conducted. The adsorption of lead on HB conforms to the H- or L-type isotherm [32]. The removal of Pb^{2+} increases sharply at the low Pb^{2+} initial concentration, then levels off, and last tends to keep stable and approaches a maximum as the equilibrium Pb^{2+} concentration increases. The isothermal curves of Pb^{2+} adsorbed by Co-doped samples are the same stream as HB, all showing high affinity, but the former have greater adsorption capacity (Fig. 6 and Table 4).

The Langmuir equation is as follows:

$$Y = \frac{A_{max}KC}{1+KC}$$

where Y is the amount of lead adsorbed, A_{max} the maximum capacity, C the equilibrium concentration of the adsorbate, and K a constant related to the adsorption energy as function of temperature and adsorption enthalpy [33]. The adsorption capacities are listed in Table 4. HB has a capacity of 2538 mmol lead per kilogram mineral, which shows the high affinity of this material for Pb^{2+} [16,34]. Co-doping enhanced the removal of lead from solution. The maximum capacity of Pb^{2+} removal by doped samples increases from 2798 mmol kg^{-1} to 3146 mmol kg^{-1}. CoB20 accommodates ~24% more Pb^{2+} than HB. Furthermore, the as-

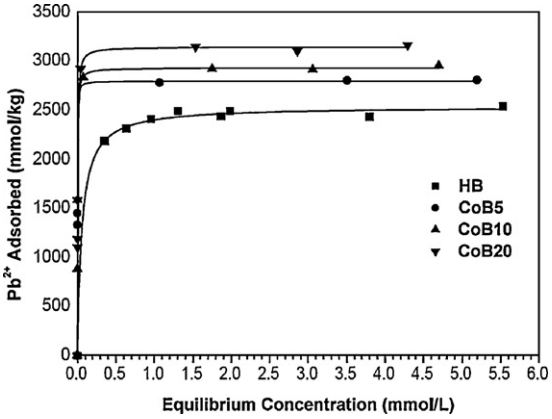

Fig. 6. Isothermal curves of Pb^{2+} uptake for Co-doped birnessites.

prepared materials adsorbed more Pb^{2+} than the other manganese oxides, such as K-birnessite (1320–2457 mmol kg^{-1}), Na-birnessite (524–1814 mmol kg^{-1}), todorokite (284.3 mmol kg^{-1}), cryptomelane (292.8 mmol kg^{-1}) and hausmannite (105.3 mmol kg^{-1}) [16,34].

The mechanisms of Pb^{2+} adsorbed by birnessites were documented in the literature. Pb^{2+} was mainly retained as an inner-sphere surface complex on octahedral vacancy sites [35–37]. Villalobos et al. [38] suggested that Pb^{2+} adsorbed by birnessite can form two different complexes, one residing in the interlayers of a crystallite to form a triple-corner-sharing (TCS) complex above/below vacant sites and the other residing on external surfaces to be a double-corner-sharing (DCS) complex at the particle

Table 4
Langmuir parameters for the adsorption of Pb^{2+} and maximum concentrations of Mn^{2+}, Co^{2+}, H^+ and K^+ released.

Sample	Parameters			Ions released (mmol kg^{-1})			
	A_{max} (mmol kg^{-1})	K	R^2	Co^{2+}	Mn^{2+}	H^+	K^+
HB	2538	17.7	0.998	0	0	2778	1283
CoB5	2798	1018.3	0.999	14.6	0	3081	1396
CoB10	2932	413.9	0.999	17.0	0	3246	1545
CoB20	3146	294.9	0.999	24.5	0	3624	1710

edges. Mn oxide crystallites are small enough in most cases that the external edge surfaces play a more important role than the vacancies. However, in our experiments, the specific surface areas of the tested materials are less than 30 m^2 g^{-1}. Compared to the adsorption on external surfaces, the adsorption on the interlayer sites may contribute to most of the Pb^{2+} retention. The increase in the lead adsorption of doped materials over HB was probably loaded above/below the vacancies, which induced the release of more protons (Table 4).

There were several reasons for the enhanced lead removal of Co-doped birnessites. Both the chemical analysis and XPS verify the decrease of the Mn AOS in Co-doped samples. This result indicates that some layer Mn^{4+} was substituted by Co^{3+}, leading to the gain of negative charge of the layer and the increase of the hydroxyl group, which contributed to the higher adsorption capacity of Pb^{2+} for doped samples than that for undoped birnessite. Also, because of the heterogeneity of Co^{3+} and $Mn^{3+/4+}$, the insertion of cobalt into the lattice of birnessite may possibly induce new vacancies [39]. The more vacancies in the birnessite, the larger are the amounts of lead that can be adsorbed [16].

During adsorption, Mn^{2+}, Co^{2+}, H^+ and K^+ are released into the solution simultaneously. As the reaction continues, the release of Co^{2+}, H^+ and K^+ is linearly increased with Pb^{2+} adsorption, while no Mn^{2+} is detected. The amount of H^+ released varies from 2778 mmol kg^{-1} to 3624 mmol kg^{-1}, and then K^+ from 1283 to 1710 mmol kg^{-1}. The Co^{2+} released is minimal (0–24.5 mmol kg^{-1}). It is suggested that almost all the cobalt exactly incorporated into the layer of the birnessite, and the negative charge of layer is mainly balanced by H^+ and K^+.

3.7. Effects of cobalt doping on the removal of As(III)

To investigate the effect of cobalt doping on the oxidation properties of birnessite, the as-prepared composites were used to study the oxidative transformation of sodium arsenite at the interface of minerals and water. Arsenite oxidation occurred quickly and was accompanied by the adsorption and fixation of As(III) and As(V), as illustrated in Fig. 7. It shows that the total arsenic and As(III) in solution decreased sharply at early reaction stages, and then slowed (Fig. 7a and b). The decrease in the total arsenic concentration in

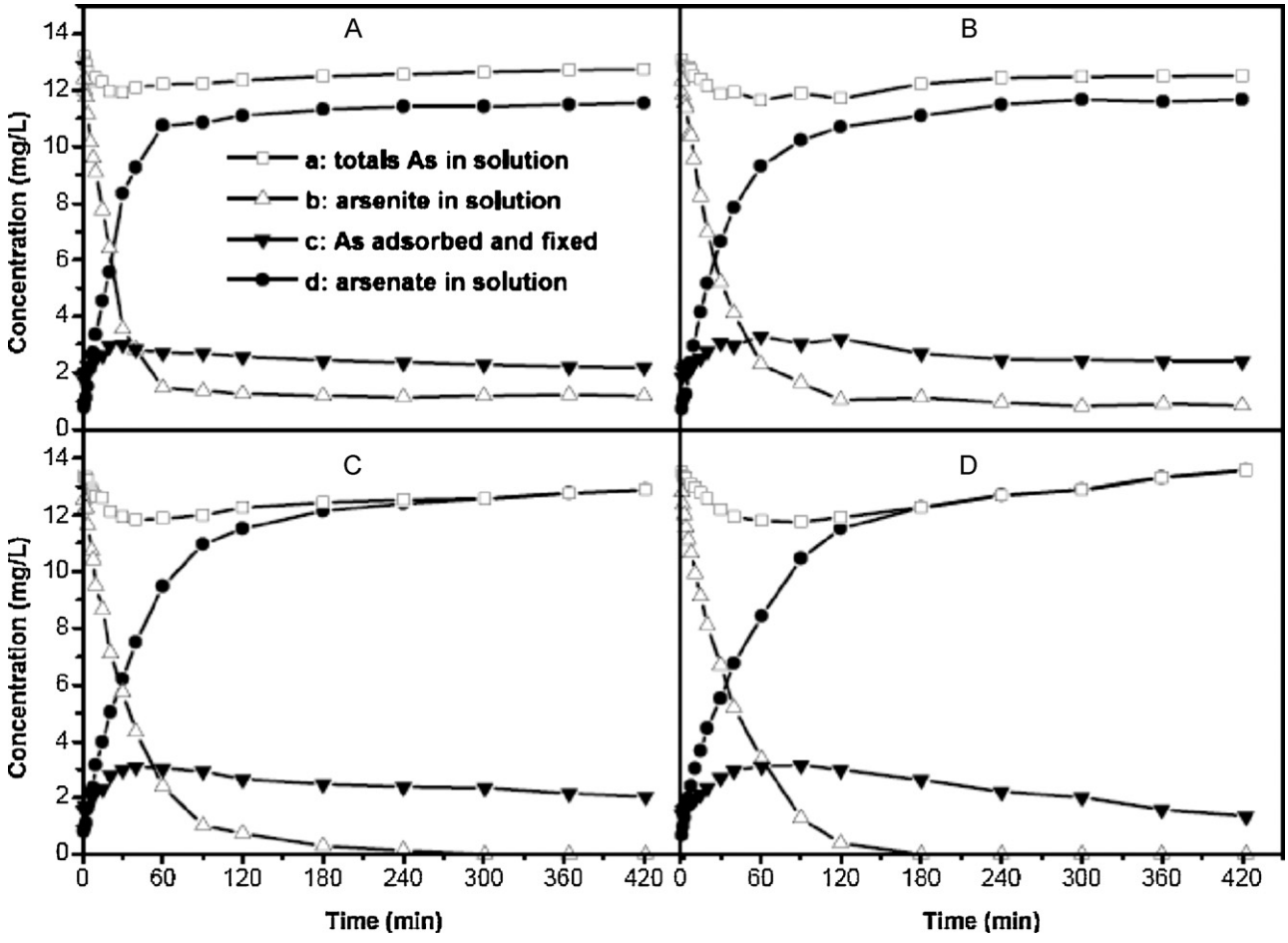

Fig. 7. Curves of As(III) removal by Co-doped birnessites. A: HB; B: CoB5; C: CoB10; D: CoB20.

the solution was ascribed to the adsorption and fixation of As on the birnessites. For As(III) in solution, both the adsorption and oxidation by MnO_2 compensated for the decrease. The yield of As(V) in solution first increased rapidly; then, the rate gradually decreased, and equilibrated after 120–180 min (Fig. 7d).

As illustrated in Fig. 7, the initial rate for the yield of As(V) in solution is slightly higher for HB than for Co-doped ones. This was ascribed to the effects of cobalt on the reactivity of birnessites. Due to the high CFSE of the low-spin Co^{3+} ion, oxygen atoms bound to Co^{3+} will be more strongly held than those bound to $Mn^{3+/4+}$. This would increase the activation energy at these sites, resulting in a slower reaction rate [40,41]. However, the total oxidation capacity was enhanced after doping. Some arsenite was unoxidized by HB and CoB5, whereas no residual arsenite in solution was observed for CoB10 and CoB20. This positive effect was also observed in the catalytic activity with respect to the olefin oxidation of Co-doped manganese oxides [10]. The higher standard redox potential of Co^{3+}/Co^{2+} ($E^0 = 1.92$ V) than those of MnO_2/Mn^{2+} ($E^0 = 1.224$ V) and Mn^{3+}/Mn^{2+} ($E^0 = 1.542$ V) may be an important reason for the improved oxidation ability [42]. The XPS investigation of the spent materials obviously shows the Co^{2+} signal (Fig. S2, a) [27].

From Fig. 7c, we can further see that the content of As adsorbed and fixed on the birnessites first increases to a maximum, then decreases slowly. Once the arsenite was mixed with the birnessite, H_3AsO_3 ($pK = 9.29$) [42] quickly adsorbed on the surface of the materials. As the reactions went on, arsenite was oxidized to arsenate. At the circumneutral pH, electronic repulsion between species, such as $H_2AsO_4^-$ and $HAsO_4^{2-}$ (H_3AsO_4, $pK_1 = 2.26$, $pK_2 = 6.76$, $pK_3 = 11.29$) [42], and the negative charge surfaces of birnessites drove them away. However, the As fixed by the minerals may remain constant, as presented by Li et al. [17]. At the end of the reaction, there were solely small amounts of exchangeable arsenate adsorbed on the surfaces. They were 0.068, 0.076, 0.085 and 0.067 mg L^{-1} arsenate for HB, CoB5, CoB10 and CoB20, respectively. Amounts of As fixed by as-prepared birnessites were 2.130, 2.336, 1.95 and 1.276 mg L^{-1}, respectively. The total removal of As(III) from solution, including the oxidation, adsorption and fixation, by Co-doped birnessites was 94.30%, 100% and 100%, respectively, compared to that of HB at 92.03%. As reported previously, ferruginous manganese ore can remove approximately 99% of arsenic from real groundwater samples [43]. Our as-prepared composites with higher cobalt content are more efficient removal reagents than the ferruginous manganese ore.

During the arsenite oxidation, contents of Mn^{4+} on the surface of the spent composites decreased, while those of $Mn^{3+/2+}$ increased and both Co^{2+} and Co^{3+} coexisted on the surface (Fig. S2). We also monitored the release of Mn^{2+}, Co^{2+} and K^+ into the solution. The K^+ released by HB, CoB5, CoB10 and CoB20 during arsenite transformation was 1998, 1931, 1900, 1814 mmol kg^{-1}, respectively. However, Mn^{2+} and Co^{2+} were not detected. There were several reasons for these phenomena. First, the spent Co-doped birnessites remained the basic layer structure (Fig. S3). As the high affinity for Pb^{2+} of the as-synthesized materials discussed previously, Mn^{2+} and Co^{2+}, the reduction products of high valence manganese and cobalt, were retained at the mineral surfaces by adsorption [17,44]. The precipitations of $Co_3(AsO_4)_2$ ($K_{sp} = 6.80 \times 10^{-29}$) [42] and the possible formation of krautite [45] may be the other reasons.

4. Conclusion

Nano-sized Co-doped birnessites were synthesized at atmospheric pressure and characterized by powder XRD, chemical analysis, N_2 adsorption, FE-SEM and XPS. Their behaviors of lead adsorption and arsenite removal were also investigated. The following results were obtained:

- Co-doped birnessites have the same crystal structure and micromorphology with undoped ones, but slightly weaker crystallinity.
- The content of Mn in the Co-doped materials decreases, and K remains unvaried as the initial molar ratios of Co/Mn increase. Additionally, the Mn AOS gradually decreases.
- XPS analyses show that cobalt exists mainly as Co(III)OOH in the structure, and Co-doped samples have a higher abundance of hydroxyl groups than undoped materials.
- Co-doped birnessite is a good scavenger for Pb^{2+} and As(III). It is promising that manganese oxides can be doped with other first row transition metals (V, Cr, Fe, Co, Ni and others) to strengthen their potential to be used in the remediation of water or soil polluted by inorganic toxic ions.

Acknowledgements

The authors gratefully thank the National Natural Science Foundation of China (Nos. 40830527 and 40771102), the Foundation for the Author of National Excellent Doctoral Dissertation of PR China (No. 200767) and the Program for New Century Excellent Talents in University (No. NCET-09-0399) for financial support.

Appendix A. Supplementary data

Supplementary data associated with this article can be found, in the online version, at doi:10.1016/j.jhazmat.2011.01.129.

References

[1] S.L. Suib, Structure, porosity, and redox in porous manganese oxide octahedral layer and molecular sieve materials, J. Mater. Chem. 18 (2008) 1623–1631.
[2] Yu.N. Vodyanitskii, Mineralogy and geochemistry of manganese: a review of publications, Eurasian Soil Sci. 42 (2009) 1170–1178.
[3] R.P. Han, W.H. Zou, Z.P. Zhang, J. Shi, J.J. Yang, Removal of copper(II) and lead(II) from aqueous solution by manganese oxide coated sand. I. Characterization and kinetic study, J. Hazard. Mater. B137 (2006) 384–395.
[4] R.P. Han, W.H. Zou, H.K. Li, Y.H. Li, J. Shi, Copper(II) and lead(II) removal from aqueous solution in fixed-bed columns by manganese oxide coated zeolite, J. Hazard. Mater. B137 (2006) 934–942.
[5] E. Eren, B. Afsin, Y. Onal, Removal of lead ions by acid activated and manganese oxide-coated bentonite, J. Hazard. Mater. 161 (2009) 677–685.
[6] J. Pakarinen, R. Koivula, M. Laatikainen, K. Laatikainen, E. Paatero, R. Harjula, Nanoporous manganese oxides as environmental protective materials–effect of Ca and Mg on metals sorption, J. Hazard. Mater. 180 (2010) 234–240.
[7] H. Zhou, J.Y. Wang, X. Chen, C.L. O'Young, S.L. Suib, Studies of oxidative dehydrogenation of ethanol over manganese oxide octahedral molecular sieve catalysts, Micropor. Mesopor. Mater. 21 (1998) 315–324.
[8] X. Chen, Y.F. Shen, S.L. Suib, C.L. O'Young, Characterization of manganese oxide octahedral molecular sieve (M-OMS-2) materials with different metal cation dopants, Chem. Mater. 14 (2002) 940–948.
[9] C. Calvert, R. Joesten, K. Ngala, J. Villegas, A. Morey, X.F. Shen, S.L. Suib, Synthesis, characterization, and Rietveld refinement of Tungsten-framework-doped porous manganese oxide (K-OMS-2) material, Chem. Mater. 20 (2008) 6382–6388.
[10] S.H. Lee, T.W. Kim, D.H. Park, J.H. Choy, S.J. Hwang, Single-step synthesis, characterization, and application of nanostructured $K_xMn_{1-y}Co_yO_{2-\delta}$ with controllable chemical compositions and crystal structures, Chem. Mater. 19 (2007) 5010–5017.
[11] A. Ogata, S. Komaba, R. Baddour-Hadjean, N. Kumagai, Doping effects on structure and electrode performance of K-birnessite-type manganese dioxides for rechargeable lithium battery, Electrochim. Acta 53 (2008) 3084–3093.
[12] Y.F. Yao, N. Gupta, H.S. Wroblowa, Rechargeable manganese oxide electrodes. Part I. Chemically modified materials, J. Electroanal. Chem. 223 (1987) 107–117.
[13] H.S. Wroblowa, N. Gupta, Rechargeable manganese oxide electrodes. Part II. Physically modified materials, J. Electroanal. Chem. 238 (1987) 93–102.
[14] S.M. Webb, B.M. Tebo, J.R. Bargar, Structural characterization of biogenic Mn oxides produced in seawater by the marine *Bacillus* sp. strain SG-1, Am. Miner. 90 (2005) 1342–1357.
[15] R.M. McKenzie, The synthesis of birnessite, cryptomelane, and some other oxides and hydroxides of manganese, Miner. Mag. 38 (1971) 493–503.
[16] W. Zhao, H.J. Cui, F. Liu, W.F. Tan, X.H. Feng, Relationship between Pb^{2+} adsorption and average Mn oxidation state in synthetic birnessites, Clay Clay Miner. 57 (2009) 513–520.
[17] X.J. Li, C.S. Liu, F.B. Li, Y.T. Li, L.J. Zhang, C.P. Liu, Y.Z. Zhou, The oxidative transformation of sodium arsenite at the interface of δ-MnO_2 and water, J. Hazard. Mater. 173 (2010) 675–681.

[18] M.A. Vieira, B. Welz, A.J. Curtius, Determination of arsenic in sediments, coal and fly ash slurries after ultrasonic treatment by hydride generation atomic absorption spectrometry and trapping in an iridium-treated graphite tube, Spectrochim. Acta B 57 (2002) 2057–2067.
[19] D.W. Oscarson, P.M. Huang, W. Liaw, The oxidation of arsenite by aquatic sediments, J. Environ. Qual. 9 (1980) 700–703.
[20] N. Kijima, H. Yasuda, T. Sato, Y. Yoshimura, Preparation and characterization of open tunnel oxide α-MnO_2 precipitated by ozone oxidation, J. Solid State Chem. 159 (2001) 94–102.
[21] H.W. Nesbitt, G.W. Canning, G.M. Bancroft, XPS study of reductive dissolution of 7 Å-birnessite by H_3AsO_3, with constraints on reaction mechanism, Geochim. Cosmochim. Acta 62 (1998) 2097–2110.
[22] R.M. Mckenzie, The reaction of cobalt with manganese dioxide minerals, Aust. J. Soil Res. 8 (1970) 97–106.
[23] R.D. Shannon, Revised effective ionic radii and systematic studies of interatomic distances in halides and chalcogenides, Acta Crystallogr. A 32 (1976) 751–767.
[24] X.J. Jiang, D. Yao, X.H. Lin, S.K. Zhai, Factors controlling the distribution of transitional metal elements in marine hydrogenic ferromanganese crusts, J. Ocean Univ. Chin. (Ocean. Coast. Sea Res.) 8 (2009) 57–64.
[25] J.L. Chen, J. Li, H.J. Li, X.M. Huang, W.J. Shen, Facile synthesis of Ag-OMS-2 nanorods and their catalytic applications in CO oxidation, Micropor. Mesopor. Mater. 116 (2008) 586–592.
[26] D.L. Crowther, J.G. Dillard, J.W. Murray, The mechanism of Co(I1) oxidation on synthetic birnessite, Geochim. Cosmochim. Acta 47 (1983) 1399–1403.
[27] B.J. Tan, K.J. Klabunde, P.M.A. Sherwood, XPS studies of solvated metal atom dispersed (SMAD) catalysts, evidence for layered cobalt–manganese particles on alumina and silica, J. Am. Chem. Soc. 113 (1991) 855–861.
[28] C.A. Strydom, H.J. Strydom, X-ray photoelectron spectroscopy studies of some cobalt(II) nitrate complexes, Inorg. Chim. Acta 159 (1989) 191–195.
[29] F.A. Cotton, G. Wilkinson, Advanced Inorganic Chemistry, 3rd ed., John Wiley & Sons, New York, 1972.
[30] S.W. Knipe, J.R. Mycroft, A.R. Pratt, H.W. Nesbitt, G.M. Bancroft, X-ray photoelectron spectroscopic study of water adsorption on iron sulphide minerals, Geochim. Cosmochim. Acta 59 (1995) 1079–1090.
[31] J. Portier, G. Campet, J. Etourneau, B. Tanguy, A simple model for the estimation of electronegativities of cations in different electronic states and coordinations, J. Alloys Compd. 209 (1994) 285–289.
[32] C.H. Giles, T.H. MacEwan, S.N. Nakhwa, D. Smith, Studies in adsorption. Part XI. A system of classification of solution adsorption isotherms and its use in diagnosis of adsorption mechanisms and in measurement of specific surface area of solids, J. Chem. Soc. 3 (1960) 3973–3993.
[33] D.G. Kinniburgh, General purpose adsorption isotherms, Environ. Sci. Technol. 20 (1986) 895–904.
[34] X.H. Feng, L.M. Zhai, W.F. Tan, F. Liu, J.Z. He, Adsorption and redox reactions of heavy metals on synthesized Mn oxide minerals, Environ. Pollut. 147 (2007) 366–373.
[35] C.J. Matocha, E.J. Elzinga, D.L. Sparks, Reactivity of Pb(II) at the Mn(III,IV) (oxyhydr)oxide–water interface, Environ. Sci. Technol. 35 (2001) 2967–2972.
[36] J.R. Bargar, G.E. Brown Jr., G.A. Parks, Surface complexation of Pb(II) at oxide–water interfaces. I. XAFS and bond-valence determination of mononuclear and polynuclear Pb(II) sorption products on aluminum oxides, Geochim. Cosmochim. Acta 61 (1997) 2617–2637.
[37] A. Manceau, B. Lanson, V.A. Drits, Structure of heavy metal sorbed birnessite. Part III. Results from powder and polarized extended X-ray absorption fine structure spectroscopy, Geochim. Cosmochim. Acta 66 (2002) 2639–2663.
[38] M. Villalobos, J. Bargar, G. Sposito, Mechanisms of Pb(II) sorption on a biogenic manganese oxide, Environ. Sci. Technol. 39 (2005) 569–576.
[39] M. Polverejan, J.C. Villegas, S.L. Suib, Higher valency ion substitution into the manganese oxide framework, J. Am. Chem. Soc. 126 (2004) 7774–7775.
[40] R.M. Mckenzie, The influence of cobalt on the reactivity of manganese dioxide, Aust. J. Soil Res. 9 (1971) 55–58.
[41] R.G. Burns, Mineralogical Applications of Crystal Field Theory, 2nd ed., Cambridge University Press, Cambridge, 1993.
[42] D.R. Lide, W.M. "Mickey" Haynes, Handbook of Chemistry and Physics, 19th ed., CRC Press/Taylor and Francis, Florida, 2010.
[43] S. Chakravarty, V. Dureja, G. Bhattacharyya, S. Maity, S. Bhattachavjee, Removal of arsenic from groundwater using low cost ferruginous manganese ore, Water Res. 36 (2002) 625–632.
[44] A.T. Stone, H.J. Ulrich, Kinetics and reaction stoichiometry in the reductive dissolution of manganese(IV) dioxide and Co(III) oxide by hydroquinone, J. Colloid. Interf. Sci. 132 (1989) 509–522.
[45] C. Tournassat, L. Charlet, D. Bosbach, A. Manceau, Arsenic(III) oxidation by birnessite and precipitation of manganese(II) arsenate, Environ. Sci. Technol. 36 (2002) 493–500.